Disturbance Decoupling in Grid-Forming Inverters for Enhanced Dynamic Response

Amiron W. dos S. Serra[1,*], Luiz A. de S. Ribeiro[1], Mehdi Savaghebi[2]

[1]Institute of Electrical Energy, Federal University of Maranhão, São Luís - Maranhão, Brazil.
[2]Department of Engineering Technology, Technical University of Denmark, Ballerup, Denmark.

e-mail: amiron.wolff@discente.ufma.br*; l.a.desouzaribeiro@ieee.org; medi@dtu.dk.
*Corresponding author.

ABSTRACT This paper presents a control strategy for grid-forming inverters, utilizing a cascaded dual-control scheme that integrates current and voltage controllers, along with an outer loop for regulating the injected active and reactive power. The proposed approach enhances system performance by addressing key challenges faced by grid-forming inverters. One of the highlights of this strategy is the improved disturbance rejection capability of the current controller, achieved through capacitor voltage decoupling. This modification effectively reduces the impact of disturbances on system performance. Additionally, the voltage controller incorporates the concept of disturbance input decoupling, which further improves the inverter's dynamic response under varying operating conditions. Notably, the inclusion of disturbance input decoupling enhances the loop gain of the voltage controller in the low-frequency range, leading to superior performance of the inverter. Experimental results validate the efficacy of the proposed control strategy in managing real-word scenarios such as voltage sags, load changes and variations in power references. These findings highlight the robustness of the proposed methodology, demonstrating its potential for enhancing the operation of grid-forming inverters in modern power systems.

KEYWORDS control strategy, grid-forming inverters, disturbance rejection capability, disturbance input decoupling.

I. INTRODUCTION

Power electronic converters play a crucial role in integrating renewable energy sources (RESs) into modern power systems, which are increasingly influenced by power electronics [1], [2]. With the rising adoption of inverter-based resources (IBRs), particularly wind and solar photovoltaic systems, as well as battery energy storage systems (BESSs), the structure of the electrical grid is undergoing significant changes. This evolution is shifting the balance between the energy demands and the services provided by the grid. As synchronous machines (SMs) are gradually replaced by IBRs, the essential services that SMs traditionally offered—such as voltage and frequency regulation—are becoming less prevalent. Consequently, it is imperative for IBRs to take on these critical functions to ensure grid stability and reliability [3]. Conventional IBRs control strategies have typically employed the grid-following (GFL) approach, and in this method, the inverter operates by synchronizing its output to the grid, fundamentally following the grid's voltage and frequency. To accomplish this, these parameters are measured at the point of common coupling (PCC) using a phase-locked loop (PLL). However, the PLL can negatively impact system stability, particularly when the grid is weak [4], [5]. Basically, the GFL IBRs are configured to operate at the rated output power and inject it into a powered grid. Power control loops are used to regulate active and reactive

power (P and Q) and to generate current references for the current control loop.

Another control strategy for IBRs is the grid-forming (GFM) approach, and according to NERC (North American Electric Reliability Corporation) the GFM IBR control can be defined as "an internal voltage phasor that is constant or nearly constant in the sub-transient to transient time frame" [6]. Although the term GFM has been widely used in recent years, its concept, which is based on regulating voltage and frequency, was proposed many years ago [7].

Among the GFM strategies, those that stand out the most are the virtual synchronous machine (VSM) [8] - [11], that emulates the behavior of a synchronous machine, adding inertia and damping of a traditional synchronous machine to IBRs; droop control [12] - [14], that adjusts P/Q power output based on local frequency/voltage deviations (P-f and Q-V droops), enabling decentralized load-sharing among distributed resources without communication; power synchronization control (PSC) [15] - [17], that enables IBRs to synchronize their output power with the grid by adjusting voltage, frequency, and phase; Virtual Oscillator Control (VOC) [18] - [20], that leverages nonlinear oscillator dynamics to self-synchronize IBRs with the grid autonomously, enabling decentralized operation without PLL; Synchronverter [21] - [24], that replicates exactly the mathematical model of a synchronous machine (electromechanical equations, flux dynamics, and excitation

control) in IBRs and Synchronous Power Controller (SPC) [25] - [27], that combines droop characteristics with virtual inertia and damping, blending static power-frequency regulation. The strategies mentioned previously have the characteristic of work either isolated or connected to the grid, and unlike the GFL inverter, the GFM inverter typically does not rely on a PLL to maintain synchronization with the grid. Instead, most reported GFM inverters use the power synchronization mechanism of synchronous machines to stay synchronized with the grid [28]. However, when the GFM inverter works connected to the grid, it is more susceptible to instability as the short circuit ratio (SCR) of the grid increases, as well as the increase in the X/R ratio of the feeders.

Many studies have been conducted with the goal of enhancing the dynamic response of GFM inverters, especially regarding reducing power oscillation. In [29], an active-damping control method based on self- and mutual-damping controllers to attenuate both self- and mutually-induced low-frequency power oscillations was proposed. In [30], it was proposed a virtual inductance control strategy to mitigate the unstable oscillation of frequency and powers, which differs from conventional virtual inductance strategies in that it does not dependent on a dual-loop control architecture. In [31], it was implemented virtual reactance instead of using virtual resistance to dampen the low-frequency resonance of the GFM inverter. The work presented in [32] decided to use a distinct solution based on artificial intelligence to predict oscillation modes and enhance damping of electromechanical inter-areas oscillations. Basically, the strategy presented in [33] aims to predict and adaptively tune a dedicated loop of the SPC to damp oscillations and enhance system stability. In [34], it was proposed a control strategy using virtual damping for enhancing the system damping and virtual reactance to suppress oscillations without altering the synchronverters' fundamental characteristics. In [35], it was proposed a strategy based on virtual damper winding applied to GFM inverter to decrease the low-frequency oscillations, utilizing existing state variables without requiring a PLL. In [36], it was proposed a generic voltage control scheme for GFM inverters that enhances voltage tracking and power regulation

in both grid-tied and stand-alone modes, addressing conflicts in power loop dynamics and improving overall system stability and performance.

In these works, the investigation was carried out almost entirely on the power control loops, without a deep analysis of the inner loops to improve the dynamic response of the GFM inverter. In light of the above, this paper aims to develop a control strategy for GFM inverters, focusing on the inner loops design (current and voltage control loops) to improve the dynamic response of the inverter. The main contributions of this work are:

1) A current control loop with high-bandwidth and disturbance decoupling, which allows enhanced disturbance rejection capability, in situations such as voltage sags.

2) A voltage control loop with disturbance input decoupling, which reduces oscillations in the inverter's electrical parameters, specifically improving active power, reactive power, and current.

This paper is an extension of the conference paper in [37] by the same authors. In this extended version, the mathematical development is presented in greater detail, and experimental results are included to complement the theoretical analysis. The paper is organized as follows: Section II outlines the system description, highlighting each of the parameters that are part of the model. Section III presents a detailed development of the modified inner loops (current and voltage loops). Section IV presents experimental results to validate theoretical development. Finally, Section V concludes this paper.

II. SYSTEM DESCRIPTION

The topology of a GFM inverter for grid-connected operation, incorporating an LCL filter and inner control loops for current and voltage, is depicted in Fig. 1. The DC-link voltage is represented by V_{dc}, grid voltage by v_g, capacitor voltages by v_c, grid-side currents by i_g, capacitor currents by i_c and voltages at the PCC by v_{pcc}. The filter parameters are as follows: L_1 is the converter-side inductor, C is the filter capacitor, L_2 is the grid-side inductor, and r_1 and r_2 are the
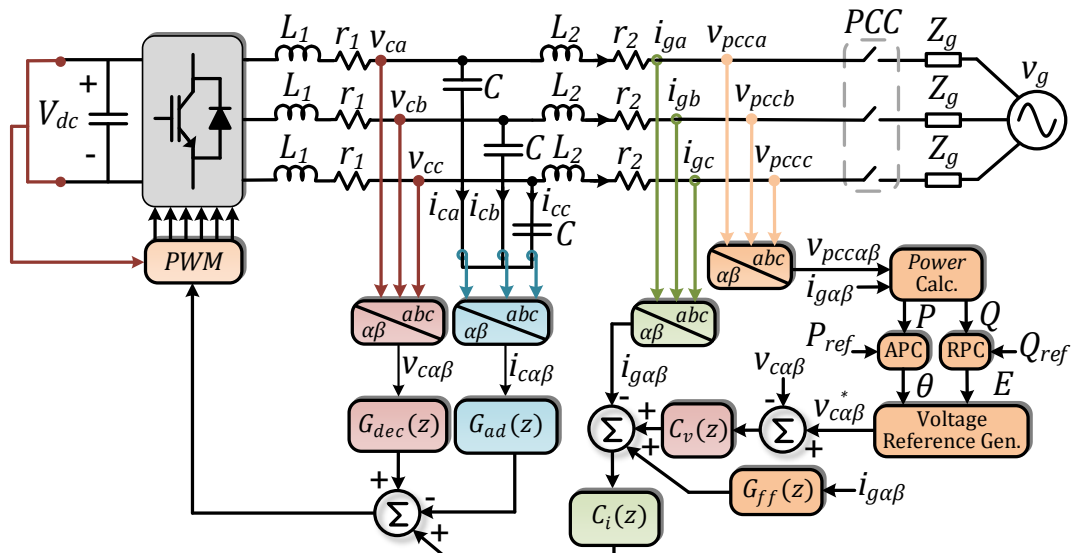

FIGURE 1. Topology of a three-phase GFM inverter.

equivalent series resistance (ESR) of L_1 and L_2, respectively. The grid impedance is represented by Z_g.

The outer loops are represented by the active power controller (APC) and the reactive power controller (RPC). The former aims to control the active power (P), with the active power reference represented by P_{ref} and generates the phase reference at the output, represented by θ. The latter aims to control the reactive power (Q), with the reactive power reference represented by Q_{ref} and generates the voltage magnitude reference at the output, represented by E. The parameters θ and E together determine the reference voltage in the $\alpha\beta$ coordinate system, $v_{c\alpha\beta}$, for the capacitor voltage controller $C_v(z)$, which is a PR controller. The transfer function $G_{ff}(z)$ is incorporated into the voltage loop to enhance the dynamic performance of the GFM inverter, and its details will be discussed in Section III-B.

The injected current i_g is regulated by a P controller $C_i(z)$, utilizing capacitor current feedback for active damping and capacitor voltage decoupling. The capacitor current i_c is fed back through the active damping transfer function $G_{ad}(z)$ to suppress the effects of the resonance frequency f_r, while v_c is decoupled using the transfer function $G_{dec}(z)$ to enhance the disturbance rejection capabilities of the current controller. The system parameters depicted in Fig. 1 are detailed in Table I. Fig. 2 presents the control block diagram of the closed-loop system for the proposed GFM inverter, excluding the power control loops. The computational delay is one sampling period (T_s), and it is modeled as z^{-1}. The PWM delay is represented by the zero-order hold (ZOH).

Table I. System Parameters

Parameter	Value
DC-link voltage (v_{dc})	650 V
Grid line voltage (RMS) (v_g)	380 V
Grid frequency (f_g)	60 Hz
Inductor (L_1)	1 mH
Inductor (L_2)	300 μH
ESR (R_1)	0.1 Ω
ESR (R_2)	0.1 Ω
Capacitor (C)	15 μF
Sample period (T_s)	100 μs
Switching frequency (f_{sw})	10 kHz

III. INNER LOOP CONTROLLERS DESIGN

This section will discuss the design of the current and voltage controllers, as well as the enhancements they will bring to the operation of the GFM inverter.
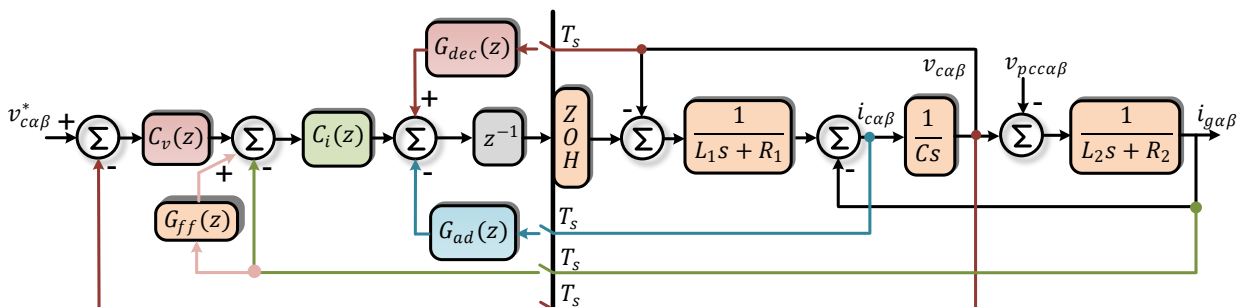
A. DESIGN OF THE CURRENT CONTROLLER

The injected current is controlled by a lead compensator, whose transfer function is given by (1). R_a is the proportional gain, and k_L [38] is the lead gain designed to reduce the effects of computational delay.

$$C_i(z) = \frac{R_a}{1 + k_L z^{-1}} \tag{1}$$

The complete transfer function of the LCL filter, which relates i_g to the terminal voltage v_{inv} of the inverter, is given by (2). However, to simplify the tuning of R_a, the filter is approximated by an equivalent L filter, where the total inductance L_T is the sum of L_1 and L_2, and the total ESR r_T is the sum of r_1 and r_2 [39], [40]. The simplified transfer function is given by (3).

$$\frac{i_g(s)}{v_{inv}(s)} = \frac{1}{\begin{array}{c}(L_1 L_2 C)s^3 + (L_1 r_2 + L_2 r_1)Cs^2 + \\ (L_1 + L_2 + r_1 r_2 C)s + r_1 + r_2\end{array}} \tag{2}$$

$$\frac{i_{g_s}(s)}{v_{inv_s}(s)} = \frac{1}{L_T s + r_T} \tag{3}$$

To validate this approximation, Fig. 3 shows the frequency response of (2) and (3). It can be noticed that up to a frequency of approximately 2 kHz, the models are equivalent. Therefore, the bandwidth of the current controller will be fixed at 2 kHz.
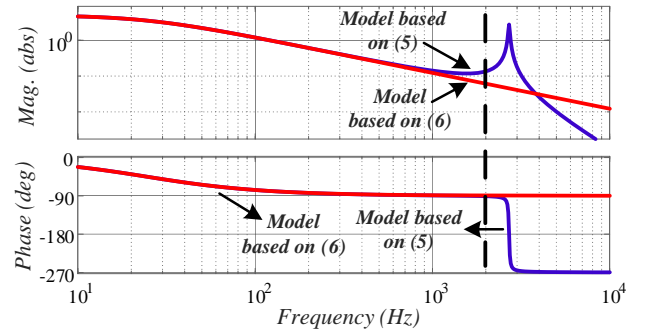

FIGURE 3. Open-loop frequency response of the *LCL* filter and the equivalent *L* filter.

The closed-loop block diagram used to control i_g is shown in Fig. 4. The model of the plant, $i_{g_s}(z)/v_{inv_s}(z)$, is given by (4), where $a = e^{-(r_T/L_T)T_s}$ and $b = (1-a)/r_T$.

$$\frac{i_{g_s}(z)}{v_{inv_s}(z)} = (1 - z^{-1})Z\left[\frac{i_{g_s}(s)}{s \cdot v_{inv_s}(s)}\right] = \frac{bz^{-1}}{1 - az^{-1}} \tag{4}$$

The closed-loop transfer function, as illustrated in Fig. 4,

FIGURE 2. GFM inverter control block diagram.

is presented in (5), with its poles required to satisfy the condition outlined in (6) [41].

$$\frac{i_{g\alpha\beta}(z)}{i_{g\alpha\beta}^*(z)} = \frac{R_a b}{(z + k_L)(z - a) + R_a b} \tag{5}$$

$$(z - p_1)(z - p_2) = (z + k_L)(z - a) + R_a b$$
$$\rightarrow z^2 - (p_1 + p_2)z + p_1 p_2 \tag{6}$$
$$= z^2 + (k_L - a)z - k_L a + R_a b$$

The closed-loop dominant poles are p_1 and p_2. By equating both sides of the equation, the parameters k_L and R_a can be determined as shown in (7) and (8), respectively.

$$k_L = a - (p_1 + p_2) \tag{7}$$

$$R_a = (p_1 p_2 + k_L a)/b \tag{8}$$
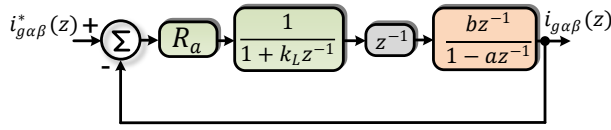
FIGURE 4. Closed-loop block diagram used for controlling i_g.

The desired locations of $p_{1,2}$ are specified in (9), while the damped natural frequency, ω_d, is defined in (10). The damping factor and the natural frequency are represented by ξ and ω_n, respectively.

$$p_{1,2} = e^{-\xi \omega_n T_s}[\cos(\omega_d T_s) \pm j\sin(\omega_d T_s)] \tag{9}$$

$$\omega_d = \omega_n \sqrt{1 - \xi^2} \tag{10}$$

The current controller bandwidth was set to 2 kHz, with $\xi = 0.9$ and $\omega_n = 2\pi \cdot 2000$ rad/s. The current controller gains are listed in Table II.

1. ACTIVE DAMPING DESIGN

As previously mentioned, the GFM inverter is connected to the grid through an *LCL*-type filter, and therefore, the resonance effect inherent to it must be mitigated. To accomplish this, a first-order lead compensator is used to increase the region of positive resistance. The function $G_{ad}(s)$ is presented in (11) [42].

$$G_{ad}(s) = \frac{1 + \tau_L s}{1 + \alpha \tau_L s} \tag{11}$$

The parameter τ_L is tuned based on (12), and the main goal of $G_{ad}(s)$ is to provide the greatest phase lead around the filter's resonance frequency ω_{res}. Therefore, the value of ω_{res} is chosen based on the filter parameters presented in Table I. The value assigned to α is 0.1 [43]. The calculated value of τ_L is $1.86 \cdot 10^{-4}$.

$$\tau_L = \frac{1}{\omega_{res}\sqrt{\alpha}} \tag{12}$$

To obtain the transfer function $G_{ad}(z)$, $G_{ad}(s)$ was discretized using the Tustin method to achieve the discrete-

time implementation, as this method provided the best approximation between the continuous and discrete time domains.

2. CAPACITOR VOLTAGE DECOUPLING DESIGN

Before moving forward with the $G_{dec}(z)$ design, the expression for the GFM inverter output impedance $Z_o(z)$ must be derived. This can be achieved through several simplifications of the block diagram presented in Fig. 5. This diagram is essentially the same as the one presented in Fig. 2, but without the voltage loop.
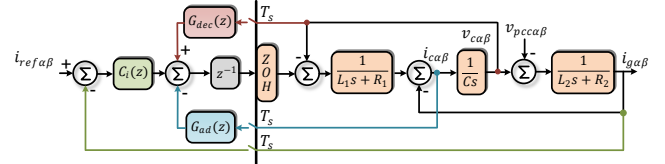

FIGURE 5. Closed-loop block diagram for the current loop.

By applying the *ZOH* discretization to the model in Fig. 5, the discrete model can be obtained as shown in Fig. 6 where $G_{vc}(z)$, $G_{ic}(z)$, $v_c(s)/v_{inv}(s)$ and $i_c(s)/v_{inv}(s)$ are defined by (13) - (16), respectively.
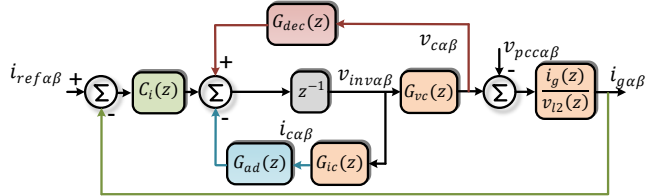

FIGURE 6. Discrete model for the closed-loop current loop block diagram.

$$G_{vc}(z) = \frac{v_c(z)}{v_{inv}(z)} = Z\left\{ZOH \cdot \frac{v_C(s)}{v_{inv}(s)}\right\} \tag{13}$$

$$G_{ic}(z) = \frac{i_c(z)}{v_{inv}(z)} = Z\left\{ZOH \cdot \frac{i_C(s)}{v_{inv}(s)}\right\} \tag{14}$$

$$\frac{v_C(s)}{v_{inv}(s)} = \frac{L_2 s + R_2}{\substack{s^3 L_1 L_2 C + s^2 C(L_1 R_2 + L_2 R_1) + \\ + s(L_1 + L_2 + CR_1 R_2) + R_1 + R_2}} \tag{15}$$

$$\frac{i_C(s)}{v_{inv}(s)} = \frac{s^2 L_2 C + s R_2 C}{\substack{s^3 L_1 L_2 C + s^2 C(L_1 R_2 + L_2 R_1) + \\ + s(L_1 + L_2 + CR_1 R_2) + R_1 + R_2}} \tag{16}$$

The transfer function $i_g(z)/v_{l2}(z)$ is defined by (17), where $i_g(z)/v_{inv}(z)$ is obtained by applying the *ZOH* discretization in (2), and $v_{l2}(z)/v_{inv}(z)$ is obtained by applying the *ZOH* discretization in (18).

$$G_{ig}(z) = \frac{i_g(z)}{v_{l2}(z)} = \frac{i_g(z)}{v_{in}(z)}\left[\frac{v_{l2}(z)}{v_{in}(z)}\right]^{-1} \tag{17}$$

$$\frac{v_{l2}(z)}{v_{inv}(z)} = Z\left\{ZOH\left[(L_2 s + R_2) \cdot \frac{i_g(s)}{v_{inv}(s)}\right]\right\} \tag{18}$$

Fig. 7 shows a simplified block diagram obtained after several modifications to the diagram presented in Fig. 6, where β is given by (19).

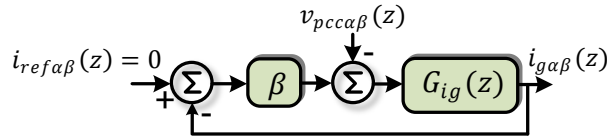$$\beta = \frac{C_i(z)G_{vc}(z)z^{-1}}{1 + [G_{ad}(z)G_{ic}(z) - G_{dec}(z)G_{vc}(z)]z^{-1}} \quad (19)$$

FIGURE 7. Simplified block diagram for the current loop.

Thus, based on (17) and (19), $Z_o(z)$ is represented by the unnumbered equation shown at the bottom of this page.

The decoupling function G_{dec} was designed to enhance the disturbance rejection capability of the current controller. It incorporates a lead-lag compensation, which consisted of a low-pass Butterworth filter in series with a lead compensator, as shown in (20).

The cutoff frequency, ω_c, of the filter was set to $2\pi \cdot 1500 \, rad/s$, and it was chosen as a compromise between stability and enhanced disturbance rejection capability. The parameters τ_z and τ_p were tuned with the help of MATLAB to compensate for the delay at the fundamental frequency (60 Hz). The values obtained were $\tau_z = 1.8041 \times 10^{-4}$ and $\tau_p = 3.4354 \times 10^{-5}$ [42]. Fig. 8 presents the frequency response of $Z_o(z)$ for the inverter, and it shows that the disturbance rejection capability of the inverter is improved when capacitor voltage decoupling is used. To obtain the model in the discrete-time domain, the transfer function $G_{dec}(s)$ was discretized using the Tustin method, which provides the best approximation between the continuous and discrete time domains.

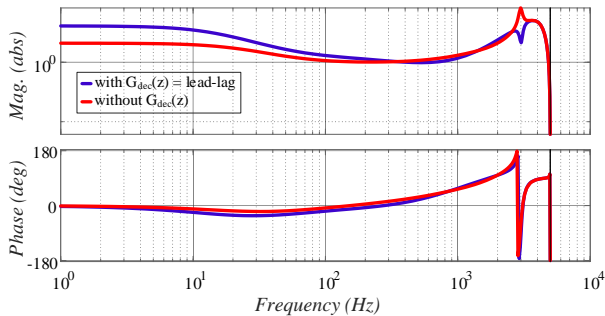$$G_{dec}(s) = \frac{\omega_c}{s + \omega_c} \cdot \frac{1 + \tau_z s}{1 + \tau_p s} \quad (20)$$

FIGURE 8. Frequency response of $Z_o(z)$ with and without $G_{dec}(z)$.

B. *DESIGN OF THE VOLTAGE CONTROLLER*

To regulate the capacitor voltage, a PR controller given by (21) is used. K_{pv}, K_{rv} and ω_o are the proportional gain, resonant gain and grid nominal frequency in rad/s, respectively.

$$C_v(z) = K_{pv} + K_{rv} \cdot T_s \cdot \frac{1 - z^{-1}\cos(\omega_o T_s)}{1 - 2z^{-1}\cos(\omega_o T_s) + z^{-2}} \quad (21)$$

The voltage controller bandwidth was set to 200 Hz, and the gain K_{pv} was determined using the root locus method [43], as described in (22). Fig. 9 shows the root locus and the corresponding K_{pv} gain for a bandwidth of 200 Hz.

$$\frac{v_c(z)}{i_c(z)} = \frac{v_c(z)}{v_{in}(z)} \left(\frac{i_c(z)}{v_{in}(z)} \right)^{-1} \quad (22)$$

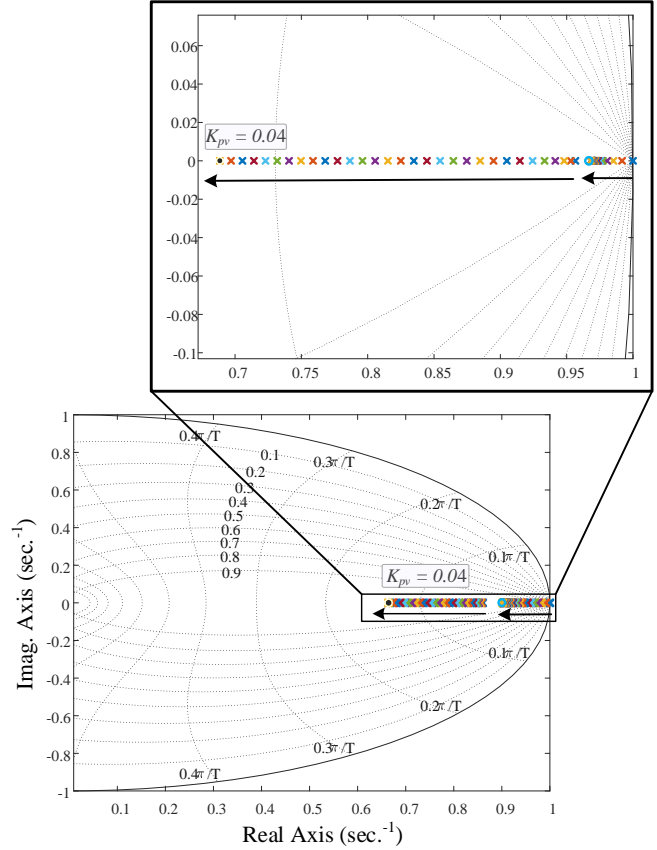where $v_c(z)/v_{in}(z)$ and $i_c(z)/v_{in}(z)$ are defined by (13) and (14), respectively.

FIGURE 9. Root locus for the voltage control loop.

The gain K_{rv} was selected based on the guideline provided in (23) [41]. The gain values are shown in Table II.

$$K_{rv} \geq 2K_{pv}\omega_o \quad (23)$$

Table II. Current and Voltage controller gains

Gain	Value
Proportional gain (R_a) – current	4.86
Lead gain (k_L)	0.22
Proportional gain (K_{pv}) – voltage	0.04
Resonant gain (K_{rv})	40

To enhance the dynamic performance of the voltage controller is used an approach based on the disturbance input decoupling (DID) method, as outlined in [44], [45]. Fig. 10 shows a block diagram of the DID implementation. Upon

$$Z_o(z) = \frac{1 + [G_{ad}(z)G_{ic}(z) - G_{dec}(z)G_{vc}(z) + C_i(z)G_{ig}(z)G_{vc}(z)]z^{-1}}{G_{ig}(z) + [G_{ig}(z)G_{dec}(z)G_{ic}(z) - G_{ig}(z)G_{dec}(z)G_{vc}(z)]z^{-1}}$$

analysis, it is evident that the $i_{g\alpha\beta}$ acts as a disturbance to the voltage control loop.

The design principle of the transfer function $G_{ff}(z)$ is to eliminate the influence of $i_{g\alpha\beta}$ at the output during sampling instants. This approach is valid only when the dynamics of the disturbance are slow compared to T_s. To satisfy this condition, it is assumed that $i_{g\alpha\beta}$ is modeled through a *ZOH* block. The expression for determining the transfer function $G_{ff}(z)$ is provided in (24). To obtain (24), it is necessary to evaluate the paths which include the disturbance and the DID transfer function.

$$-i_{g\alpha\beta}(z)\mathcal{Z}\left[ZOH \frac{1}{Cs}\right]$$
$$+ i_{g\alpha\beta}(z)G_{ff}(z)\mathcal{Z}\left[ZOH G_{CLi}(s)\frac{1}{Cs}\right] = 0 \tag{24}$$

The function $G_{CLi}(s)$ represents the current loop and, to simplify the design of the DID function, it can be approximated by an equivalent first-order system with the same bandwidth as the actual system, where $\omega_i = 2\pi \cdot 2000$ rad/s. Consequently, (24) can be reformulated as (25).

$$G_{ff}(z) = \frac{\mathcal{Z}\left[ZOH \frac{1}{Cs}\right]}{\mathcal{Z}\left[ZOH \frac{\omega_i}{s+\omega_i}\frac{1}{Cs}\right]} = K_{ff}\frac{z-\delta_z}{z-\delta_p} \tag{25}$$

The parameters δ_z, δ_p and K_{ff} are defined by (26) - (28), respectively. The calculated values are $\delta_z = 0.2846$, $\delta_p = -0.6609$ and $K_{ff} = 2.3217$.

To evaluate the impact of utilizing DID, the open-loop gain of the voltage control system shown in Fig. 2 is considered. Fig. 11 illustrates the open-loop gain of the voltage control system both with and without the proposed DID. As can be seen, the loop gain in the low-frequency range is improved when DID is used, which enhances the system's performance in the presence of disturbances.

$$\delta_z = e^{-T_s\omega_i} \tag{26}$$

$$\delta_p = \frac{\delta_z(T_s\omega_i + 1) - 1}{T_s\omega_i + \delta_z - 1} \tag{27}$$

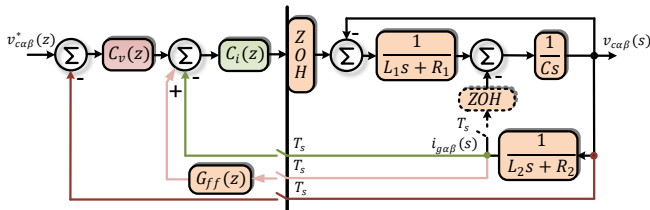$$K_{ff} = \frac{T_s\omega_i}{T_s\omega_i + \delta_z - 1} \tag{28}$$

FIGURE 10. Closed-loop block diagram to analyze the effect of $G_{ff}(z)$.

The Nyquist plot of the open-loop gain of the complete control system is shown in Fig. 12. The sensitivity peak is approximately 0.5. It can be concluded from this figure that the control system is stable since it does not encircle the critical point (-1, j0).
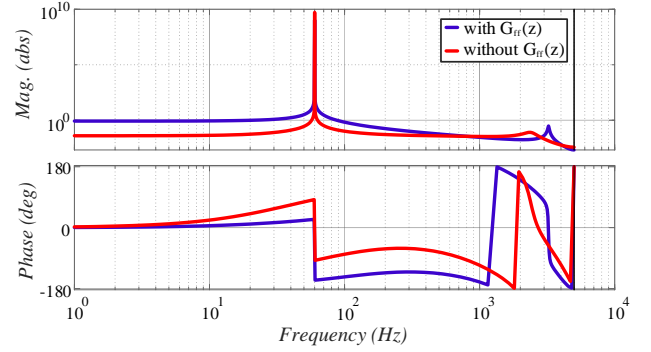
FIGURE 11. Frequency response of voltage control open-loop gain with and without $G_{ff}(z)$.
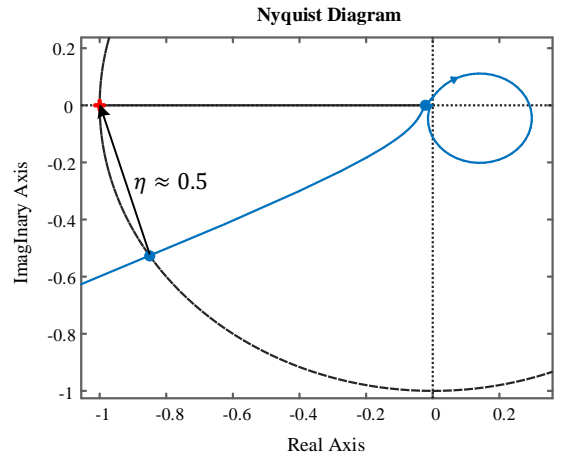
FIGURE 12. Nyquist plot of the complete control system loop gain.

IV. EXPERIMENTAL RESULTS

The proposed strategy control is verified by experimental results. The lab setup is shown in Fig. 13, and the parameters are listed in Table I. Three conditions were tested, and a grid emulator, the Chroma 61830, was used to emulate the grid. The first evaluates the performance of the current loop. In this case, only the block diagram shown in Fig. 5 is considered, with the primary objective being to analyze the influence of G_{dec}. The second condition assesses the performance of the GFM inverter operating exclusively in isolated mode, disconnected from the grid. In this scenario, the voltage reference $v_{c\alpha\beta}$ is directly imposed without any input from the power control loops. The final condition evaluates the GFM inverter operating in grid-connected mode. For this case, the topology shown in Fig. 1 is used; however, the detailed modeling of the power control loops is not addressed, as it lies outside the scope of this work.

A. CURRENT CONTROL LOOP ASSESSMENT

In this condition, it is assumed that only the current loop is active; therefore, a fixed current reference of 10 A peak is provided. The inverter injects current into the grid, and specifically for this case, a PR controller is used for the current control loop. This choice ensures zero steady-state error, allowing for the analysis of current variations around the reference value. The resonant gain is set to 10.

6

Eletrônica de Potência, Rio de Janeiro, v.30, e202528, 2025.

FIGURE 13. Lab setup for obtaining experimental results.

Fig. 14 shows the injected current in one of the phases (lilac curves) for the case without G_{dec} (Fig. 14 (a)) and with G_{dec} (Fig. 14 (b)). The voltage sag represents a 10 % reduction from the nominal line voltage value of 380 V (green curve).

By analyzing the figures, it is observed that the introduction of the decoupling function G_{dec} led to significant improvements in the dynamic response of the system. Specifically, both the overshoot and the settling time were notably reduced in the case where G_{dec} was applied. Without G_{dec}, the overshoot was measured at 1.175 A, but with G_{dec}, this overshoot decreased to 312.5 mA. This significant reduction in overshoot indicates that the inverter was able to handle the voltage sag more effectively and avoid excessive current fluctuations.

Similarly, the settling time was also improved. Without G_{dec}, the settling time was recorded at 114.8 ms. With the decoupling function applied, the settling time was reduced to 46.2 ms, indicating a much quicker recovery after the voltage dip. This shorter settling time means that the system is able to react faster to voltage disturbances, improving the overall dynamic performance.

B.   *GFM INVERTER ASSESSMENT – ISOLATED OPERATION*

In this test, the GFM inverter supplies a three-phase linear load of 17 Ω. At a certain point, another identical load is added to the system. Fig. 15 (a) and Fig. 15 (b) show the α-axis voltage reference (blue curve), with a nominal peak value of 120 V, the voltage across the capacitor in the α-axis (green curve), and the corresponding error signal (yellow curve), without and with DID, respectively.

By examining these figures, it is clear that the introduction of DID leads to a noticeable improvement in the GFM's inverter performance when responding to load changes. For the case without DID, the voltage variation observed was 53.6 V. In contrast, when DID is applied, the voltage variation decreases to 32.5 V, indicating that the GFM inverter is much better at regulating the output voltage and compensating for the additional load.

Additionally, the settling time shows a stark difference between the two scenarios. Without DID, the settling time was approximately 35 ms. With DID, however, the settling time was reduced to approximately 10 ms, reflecting a much faster recovery to the nominal operating conditions. This

reduction in settling time demonstrates the ability of DID to enhance the GFM's inverter dynamic response, ensuring that the system can react more swiftly to changes in load and return to a stable state more efficiently.
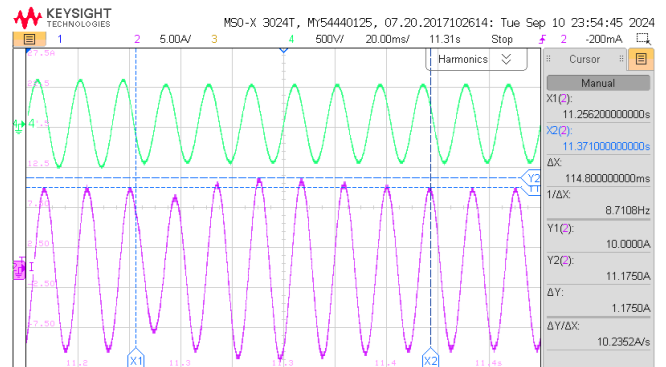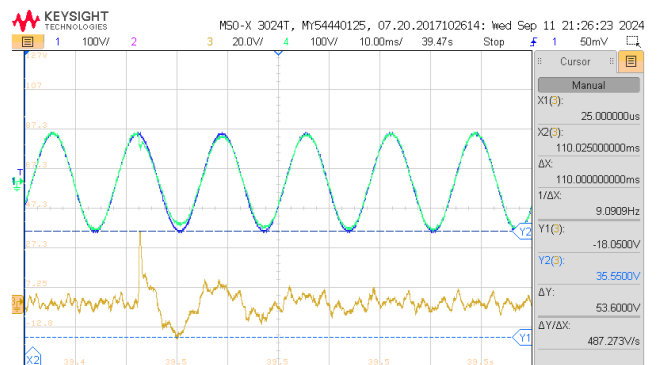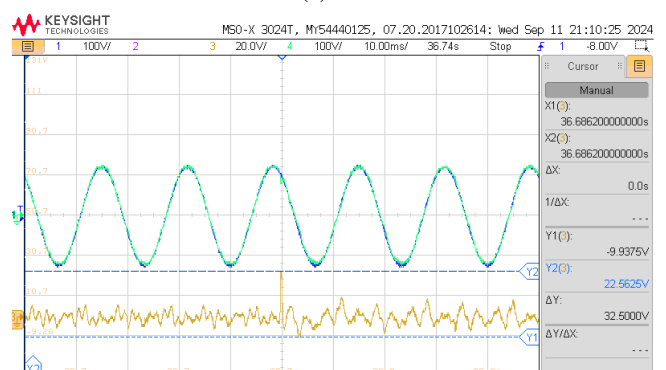

(a)
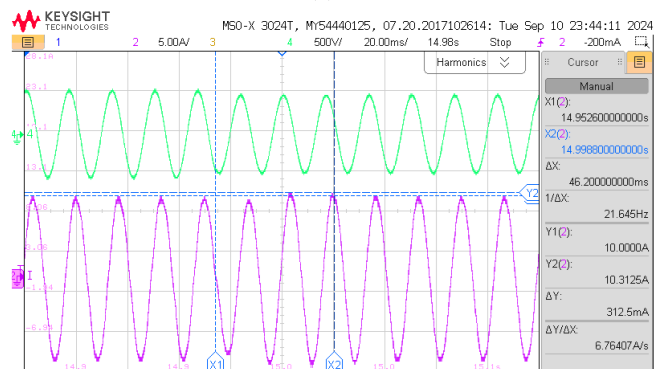
(b)

FIGURE 14. Injected current during a voltage sag: (a) without G_{dec}, (b) with G_{dec}. Lilac curves – current; Green curves – voltage.


(a)

(b)

FIGURE 15. Capacitor voltage during a load variation: (a) without DID, (b) with DID. Blue curves – $v_{c\alpha}^*$; Green curves – $v_{c\alpha}$; Yellow curves – error.

C. *GFM INVERTER ASSESSMENT – GRID-CONNECTED OPERATION*

In this test, the operation in grid-connected mode is assessed. Initially, the GFM inverter supplies 5 kW of active power and 0 kVAr of reactive power to the grid. Subsequently, the active power reference for the GFM inverter is set to 10 kW. Fig. 16 (a) and Fig. 16 (b) show the injected active power (green curve), reactive power (blue curve), and current (lilac curve), both without and with DID, respectively. The SCR of the system is 3.85, which characterizes it as a strong grid, according to [46].

From the figures, it can be observed that when DID is applied, all three parameters – active power, reactive power, and current – exhibit less oscillation at the moment the active power reference changes. Therefore, using DID improves the dynamic behavior of the GFM inverter by providing more damping, which helps control fluctuations and ensures the system stabilizes more rapidly.

(a)

(b)
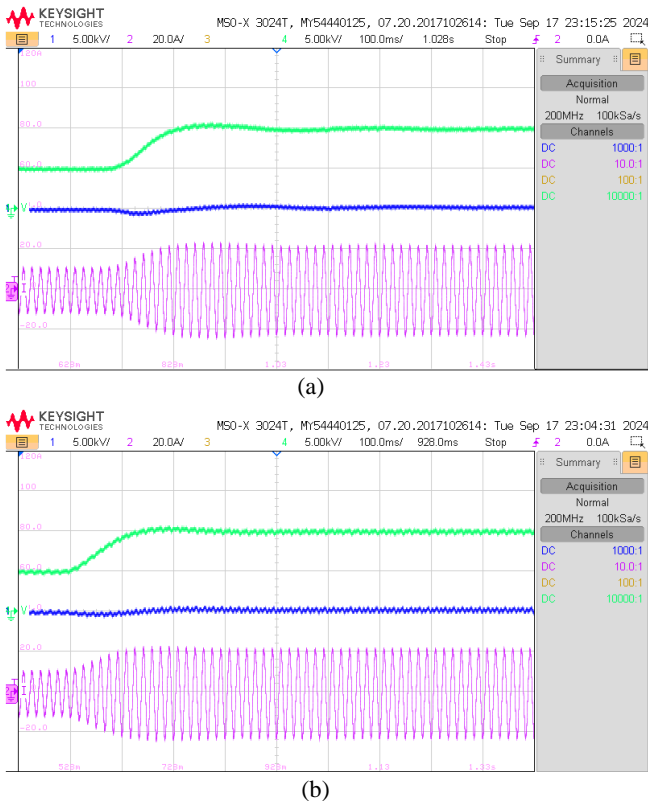
FIGURE 16. Injected active power, reactive power and current: (a) without DID, (b) with DID. Green curves – *P*; Blue curves– *Q*: Lilac curves – current.

V. CONCLUSION

This paper introduced a control strategy for a GFM inverter that incorporates a modified current control loop designed to enhance disturbance rejection capability. Additionally, a modified voltage control loop is proposed, utilizing the concept of DID applied to the injected current within the voltage control loop. The proposed approach demonstrates significant improvements in the GFM's inverter dynamic performance, particularly in scenarios involving voltage sags and load variations. Additionally, the oscillation of active power, reactive power, and current, were reduced when DID

was used in response to variations in the active power reference.

AUTHOR'S CONTRIBUTIONS

A.W.S.SERRA: Conceptualization, Formal Analysis, Investigation, Methodology, Software, Validation, Writing – Original Draft, Writing – Review & Editing. **L.A.S.RIBEIRO:** Formal Analysis, Methodology, Supervision, Writing – Review & Editing. **M.SAVAGHEBI:** Methodology, Supervision, Writing – Review & Editing.

REFERENCES

[1] Y. Yang, C. Li, L. Cheng, X. Gao, J. Xu and F. Blaabjerg, "A Generic Power Compensation Control for Grid Forming Virtual Synchronous Generator With Damping Correction Loop," *IEEE Transactions on Industrial Electronics,* vol. 71, no. 9, pp. 10908-10918, September 2024, doi: 10.1109/TIE.2023.3342332.

[2] F. Blaabjerg and K. Ma, "Future on Power Electronics for Wind Turbine Systems," *IEEE Journal of Emerging and Selected Topics in Power Electronics,* vol. 1, no. 3, pp. 139-152, September 2013, doi: 10.1109/JESTPE.2013.2275978.

[3] B. Chaudhuri, D. Ramasubramanian, J. Matevosyan, M. O'Malley, N. Miller and T. Green, "Rebalancing Needs and Services for Future Grids: System Needs and Service Provisions With Increasing Shares of Inverter-Based Resources," *IEEE Power and Energy Magazine,* vol. 22, no. 2, pp. 30-41, March-April 2024, doi: 10.1109/MPE.2023.3342113.

[4] B. Wen, D. Boroyevich, R. Burgos, P. Mattavelli e Z. Shen, "Analysis of D-Q Small-Signal Impedance of Grid-Tied Inverters," *IEEE Transactions on Power Electronics,* vol. 31, n° 1, pp. 675-687, January 2016, doi: 10.1109/TPEL.2015.2398192.

[5] D. Dong, B. Wen, D. Boroyevich, P. Mattavelli e Y. Xue, "Analysis of Phase-Locked Loop Low-Frequency Stability in Three-Phase Grid-Connected Power Converters Considering Impedance Interactions," *IEEE Transactions on Industrial Electronics,* vol. 62, n° 1, pp. 310-321, January 2015, doi: 10.1109/TIE.2014.2334665.

[6] NERC, "Grid forming technology: Bulk power system reliability considerations," North American Electric Reliability Corporation (NERC), Atlanta, USA, 2021.

[7] M. Chandorkar, D. Divan and R. Adapa, "Control of Parallel Connected Inverters in Standalone AC Supply Systems," *IEEE Transactions on Industry Applications,* vol. 29, no. 1, pp. 136-143, January/February 1993, doi: 10.1109/28.195899.

[8] S. D'Arco and J. A. Suul, "Virtual synchronous machines — Classification of implementations and analysis of equivalence to droop controllers for microgrids," in *2013 IEEE Grenoble Conference*, Grenoble, 2013, doi: 10.1109/PTC.2013.6652456.

[9] R. Heydari, M. Savagheb e F. Blaabjerg, "Virtual inertia operation of renewables," em *Control of Power Electronic Converters and Systems*, vol. 3, Academic Press, 2021, pp. 523-540, doi: 10.1016/B978-0-12-819432-4.00011-1.

[10] Y. Tian, X. Xu, Y. Wang, Z. Li, Z. Zhang e Y. Gao, "Full-State Feedback Power Decoupling Control for Grid Forming Converter With Improved Stability and Inertia Response," *IEEE Transactions On Power Electronics,* vol. 40, nº 2, pp. 2930-2942, February 2025, doi: 10.1109/TPEL.2024.3487620.

[11] C. A. P. R., J. R. Pinheiro e M. Mezaroba, "Controle de um Conversor CC-CA para Conexão à Rede com Emulação de Máquina Síncrona," *Eletrônica de Potência,* vol. 24, nº 4, pp. 470-481, December 2019, doi: 10.18618/REP.2019.4.0039.

[12] X. Meng, J. Liu and Z. Liu, "A Generalized Droop Control for Grid-Supporting Inverter Based on Comparison Between Traditional Droop Control and Virtual Synchronous Generator Control," *IEEE Transactions on Power Electronics,* vol. 34, no. 6, pp. 5416-5438, June 2019, doi: 10.1109/TPEL.2018.2868722.

[13] J. Rocabert, A. Luna, F. Blaabjerg e P. Rodriguez, "Control of power converters in AC microgrids," *IEEE Transactions on Power Electronics,* vol. 27, nº 11, p. 4734–4749, November 2012, doi: 10.1109/TPEL.2012.2199334.

[14] X. Zhao, P. G. Thakurta e D. Flynn, "Grid-forming requirements based on stability assessment for 100% converter-based Irish power system," *IET Renewable Power Generation,* vol. 16, nº 3, pp. 447-458, November 2022, doi: 10.1049/rpg2.12340.

[15] F. Zhao, T. Zhu, L. Harnefors, B. Fan, H. Wu, Z. Zhou, Y. Sun and X. Wang, "Closed-Form Solutions for Grid-Forming Converters: A Design-Oriented Study," *IEEE Open Journal of Power Electronics,* vol. 5, pp. 186-200, January 2024, doi: 10.1109/OJPEL.2024.3357128.

[16] F. Zhao, X. Wang e T. Zhu, "Power Dynamic Decoupling Control of Grid-Forming Converter in Stiff Grid," *IEEE Transactions On Power Electronics,* vol. 37, nº 8, pp. 9073-9088, August 2022, doi:10.1109/TPEL.2022.3156991 .

[17] L. Zhang, L. Harnefors e H.-P. Nee, "Power-Synchronization Control of Grid-Connected Voltage-Source Converters," *IEEE Transactions on Power Systems,* vol. 25, nº 2, pp. 809-820, May 2010, doi: 10.1109/TPWRS.2009.2032231.

[18] M. Colombino, D. Groß, J.-S. Brouillon and F. Dorfler, "Global Phase and Magnitude Synchronization of Coupled Oscillators With Application to the Control of Grid-Forming Power Inverters," *IEEE Transactions on automatic control,* vol. 64, no. 11, pp. 4496-4511, November 2019, doi: 10.1109/TAC.2019.2898549.

[19] B. Johnson, M. Rodriguez, M. Sinha e S. Dhople, "Comparison of virtual oscillator and droop control," em *IEEE 18th Workshop on Control and Modeling for Power Electronics (COMPEL),* Stanford, 2017, doi: 10.1109/COMPEL.2017.8013298.

[20] S. U. Islam e S. Kim, "Comparative Analysis of Sub-Synchronous Oscillations With Various Grid-Forming Control Schemes Under Series-Compensated Line," *IEEE Access,* vol. 12, pp. 132763 - 132772, August 2024, doi: 10.1109/ACCESS.2024.3444889.

[21] K. R. Vasudevan, V. K. Ramachandaramurthy, T. S. Babu e A. Pouryekta, "Synchronverter: A Comprehensive Review of Modifications, Stability Assessment, Applications and Future Perspectives," *IEEE Access,* vol. 8, pp. 131565 - 131589, 17 July 2020, doi: 10.1109/ACCESS.2020.3010001.

[22] Q.-C. Zhong e G. Weiss, "Synchronverters: Inverters That Mimic Synchronous Generators," *IEEE Transactions on Industrial Electronics,* vol. 58, nº 4, pp. 1259 - 1267, April 2011, doi: 10.1109/TIE.2010.2048839.

[23] C. A. Busada, S. G. Jorge e J. A. Solsona, "Shaping the Transient Behavior of Synchronverters," *IEEE Transactions on Energy Conversion,* vol. 38, nº 1, pp. 735 - 738, March 2023, doi: 10.1109/TEC.2022.3220052.

[24] B. W. França, E. L. v. Emmerik, J. F. Caldeira e M. Aredes, "Sliding Droop Control For Distributed Generation In Microgrids," *Eletrônica de Potência,* vol. 22, nº 4, pp. 429-439, December 2017, doi: 10.18618/REP.2017.4.2726.

[25] W. Zhang, A. Tarraso, J. Rocabert, A. Luna, J. I. Candela e P. Rodriguez, "Frequency Support Properties of the Synchronous Power Control for Grid-Connected Converters," *IEEE Transactions on Industry Applications,* vol. 55, nº 5, pp. 5178 - 5189, September-October 2019, doi: 10.1109/TIA.2019.2928517.

[26] A. Tarrasó, C. Verdugo, N. B. Lai, J. I. Candela e P. Rodriguez, "Synchronous Power Controller for Distributed Generation Units," em *IEEE Energy Conversion Congress and Exposition (ECCE),* Baltimore, 2019, doi: 10.1109/ECCE.2019.8912667.

[27] W. Zhang, A. M. Cantarellas, J. Rocabert, A. Luna e P. Rodriguez, "Synchronous Power Controller With Flexible Droop Characteristics for Renewable Power Generation Systems," *IEEE Transactions on Sustainable Energy,* vol. 7, nº 4, pp. 1572 - 1582, October 2016, doi: 10.1109/TSTE.2016.2565059.

[28] R. Rosso, X. Wang, M. Liserre, X. Lu and S. Engelken, "Grid-Forming Converters: Control Approaches, Grid-Synchronization, and Future Trends—A Review," *IEEE Open Journal of Industry Applications,* vol. 2, pp. 93-109, 2021, doi: 10.1109/OJIA.2021.3074028.

[29] Y. Yu, S. K. Chaudhary, G. D. A. Tinajero, L. Xu, J. C. Vasquez and J. M. Guerrero, "Active Damping for Dynamic Improvement of Multiple Grid-Tied Virtual Synchronous Generators," *IEEE Transactions on Industrial Electronics,* vol. 71, no. 4, pp. 3673-3683, April 2024, doi: 10.1109/TIE.2023.3277082.

[30] Y. Yang, J. Xu, C. Li, W. Zhang, Q. Wu, M. Wen and F. Blaabjerg, "A New Virtual Inductance Control Method for Frequency Stabilization of Grid-Forming Virtual Synchronous Generators," *IEEE Transactions on Industrial Electronics,* vol. 70, no. 1, pp. 441-451, January 2023, doi: 10.1109/TIE.2022.3148749.

[31] F. Zhao, X. Wang and T. Zhu, "Low-Frequency Passivity-Based Analysis and Damping of Power-Synchronization Controlled Grid-Forming Inverter," *IEEE Journal Of Emerging And Selected Topics In Power Electronics,* vol. 11, no. 2, pp. 1542-1554, April 2023, doi: 10.1109/JESTPE.2022.3218845.

[32] G. N. Baltas, N. B. Lai, L. Marin, A. Tarrasó and P. Rodriguez, "Grid-Forming Power Converters Tuned Through Artificial Intelligence to Damp Subsynchronous Interactions in Electrical Grids," *IEEE Access,* vol. 8, pp. 93369-93379, 2020, doi: 10.1109/ACCESS.2020.2995298.

[33] P. Rodríguez, C. Citro, J. I. Candela, J. Rocabert and A. Luna, "Flexible Grid Connection and Islanding of SPC-Based PV Power Converters," *IEEE Transactions on Industry Applications,* vol. 54, no. 3, pp. 2690 - 2702, May-June 2018, doi: 10.1109/TIA.2018.2800683.

[34] Z. Shuai, W. Huang, Z. J. Shen, A. Luo and Z. Tian, "Active Power Oscillation and Suppression Techniques Between Two Parallel Synchronverters During Load Fluctuations," *IEEE Transactions On Power Electronics,* vol. 35, no. 4, pp. 4127-4142, April 2020, doi: 10.1109/TPEL.2019.2933628.

[35] H. Yin, Z. Kustanovich, J. Lin and G. Weiss, "Synchronverters With Damper Windings to Attenuate Power Oscillations in Grids," *IEEE Journal Of Emerging And Selected Topics In Industrial Electronics,* vol. 5, no. 4, pp. 1376-1387, October 2024, doi: 10.1109/JESTIE.2024.3447462.

[36] H. Deng, J. Fang, Y. Qi, Y. Tang and V. Debusschere, "A Generic Voltage Control for Grid-Forming Converters With Improved Power Loop Dynamics," *IEEE Transactions On Industrial Electronics,* vol. 70, no. 4, pp. 3933-3943, April 2023, doi: 10.1109/TIE.2022.3176308.

[37] A. W. D. S. Serra, L. A. D. S. Ribeiro and M. Savaghebi, "A Multi-Loop Control for Grid-Forming Converters with Enhanced Dynamics," in *2024 Energy Conversion Congress & Expo Europe (ECCE Europe),* Darmstadt, 2024, doi:10.1109/ECCEEurope62508.2024.10751951 .

[38] F. d. Bosio, L. A. d. S. Ribeiro, F. D. Freijedo, M. Pastorelli e J. M. Guerrero, "Discrete-Time Domain Modeling of Voltage Source Inverters in Standalone Applications: Enhancement of Regulators Performance by Means of Smith Predictor," *IEEE Transactions on Power Electronics,* vol. 32, nº 10, pp. 8100-8114, October 2017, doi:10.1109/TPEL.2016.2632527 .

[39] P. J. D. O. Evald, R. V. Tambara e H. A. Gründling, "A Direct Discrete-Time Reduced Order Robust Model Reference Adaptive Control for Grid-Tied Power Converters with Lcl Filter," *Eletrônica de Potência,* vol. 25, nº 3, pp. 361-372, 30 September 2020, doi: 10.18618/REP.2020.3.0039.

[40] S. G. Parker, B. P. McGrath e D. G. Holmes, "Regions of active damping control for LCL filters," em *IEEE Energy Conversion*

Congress and Exposition (ECCE), Raleigh, 2012, doi: 10.1109/ECCE.2012.6342412.

[41] L. A. d. S. Ribeiro, F. D. Freijedo, F. d. Bosio, M. S. Lima, J. M. Guerrero e M. Pastorelli, "Full Discrete Modeling, Controller Design, and Sensitivity Analysis for High-Performance Grid-Forming Converters in Islanded Microgrids," *IEEE Transactions on Industry Applications,* vol. 54, nº 6, pp. 6267-6278, November/December 2018, doi: 10.1109/TIA.2018.2847635.

[42] A. W. d. S. Serra, L. A. d. S. Ribeiro e J. G. d. Matos, "An Enhanced Current Controller for Grid-Connected Inverters based on Capacitor Current Feedback Active Damping and Capacitor Voltage Decoupling," em *2023 25th European Conference on Power Electronics and Applications (EPE'23 ECCE Europe)*, Aalborg, 2023, doi: 10.23919/EPE23ECCEEurope58414.2023.10264543.

[43] G. F. Franklin, J. D. Powel e A. Emami-Naeini, Feedback Control of Dynamic Systems, vol. 6th, Prentice-Hall, 2010.

[44] R. D. Lorenz, *ME 547 - Design of Computer Control Systems (lecture notes),* Madison, Wisconsin: University of Wisconsin-Madison, 2005.

[45] J. G. d. Matos, F. S. F. e. Silva e L. A. d. S. Ribeiro, "Power Control in AC Isolated Microgrids With Renewable Energy Sources and Energy Storage Systems," *IEEE Transactions on Industrial Electronics,* vol. 62, nº 6, pp. 3490-3498, June 2015, doi: 10.1109/TIE.2014.2367463.

[46] IEEE, "IEEE Guide for Planning DC Links Terminating at AC Locations Having Low Short-Circuit Capacities, Standard 1204-1997," IEEE, New York, 1997, doi: 10.1109/IEEESTD.1997.85949.

[47] Y. Li, Y. Gu e T. C. Green, "Revisiting Grid-Forming and Grid-Following Inverters: A Duality Theory," *IEEE Transactions on Power Systems,* vol. 37, no. 6, pp. 4541-4554, November 2022, doi: 10.1109/TPWRS.2022.3151851.

BIOGRAPHIES

Amiron Wolff dos S. Serra born in 04/05/1993 in São Luís, Maranhão, Brazil, received his B.Sc. degree in Industrial Electrical Engineering from the Federal Institute of Education, Science and Technology of Maranhão (IFMA), Brazil, in 2017, and his M.Sc. degree in Electrical engineering from Federal University of Maranhão (UFMA), Brazil, in 2019. He is currently pursuing the Ph.D. degree at Federal University of Maranhão. From September 2023 to September 2024, he was a Guest Ph.D. student at Technical University of Denmark (DTU). His research interests include power electronics, control systems and microgrids. Mr. Amiron is a student member of IEEE.

Luiz Antonio de Souza Ribeiro received the M.Sc. and Ph.D. degrees from the Federal University of Paraiba, Campina Grande, Brazil, in 1995 and 1998, respectively. During the period 1996–1998 and 2004–2006, he was a Visiting Scholar and Post doctor with the University of Wisconsin, Madison, WI, USA, working on parameter estimation and sensorless control of AC machines. In 2015, he was a Research Guest at Aalborg University, Denmark, working on power converters control for microgrid applications. In 2023 he was an Otto Mønsted Visiting Professor at Technical University of Denmark (DTU), Copenhagen working on design and control of power electronic converters for Power-to-X facilities. He is currently a Full Professor with the Department of Electrical Engineering, Federal University of Maranhão, Brazil. His research interests include design and control of power electronics converters, microgrids, and renewable energy. Dr. Ribeiro received two IEEE Energy Conversion Congress and Exposition prize paper awards.

Mehdi Savaghebi received his B.Sc. degree from the University of Tehran, Iran, in 2004, and his M.Sc. and Ph.D. degrees from the Iran University of Science and Technology, Tehran, Iran, in 2006 and 2012, respectively, all in Electrical Engineering. From 2014 to 2017, he was a Postdoctoral Fellow at the Department of Energy, Aalborg University, Aalborg, Denmark, where he was an Associate Professor from 2017 to 2018. Then, he worked as an Associate Professor and Research Team Leader at the University of Southern Denmark, Odense, Denmark, for four years. Since 2022, he has been with the Department of Engineering Technology, Technical University of Denmark, Ballerup, Denmark, where he is currently serving as a Professor in Power Electronics-Enabled Power Systems and Head of the Energy Technology and Computer Science Section. His main research interests include renewable energy systems, microgrids, power quality and protection of electrical systems.